Rovedar

Research in Biotechnology and Environmental Science. 2023; 2(4): 88-101.

DOI: 10.58803/rbes.v2i4.32

http://rbes.rovedar.com/

Original Article

# The Use of Manganese-Tunable *p*-type ZnO Nanoscale for Optimized Photocatalytic Degradation of Terasil Blue from Wastewater

Auwal Yusha'u*, Siaka Abdulfatah, Kamaluddeen Sulaiman Kabo, and Abdullahi Muhammad

Department of Chemistry, Faculty of Physical Science Federal University Dutsin-Ma, Katsina State, Nigeria

*** *Corresponding author:*** Auwal Yusha'u, Department of Chemistry, Faculty of Physical Science Federal University Dutsin-Ma, Katsina State, Nigeria. Email: ayushau21@fudutsinma.edu.ng; auwalyushau2018@gmail.com

**ARTICLE INFO**

***Article History:***
Received: 25/09/2023
Revised: 21/10/2023
Accepted: 10/12/2023
Published: 25/12/2023

***Keywords:***
Box-behnken design
Mineralization
Mn-doped ZnO
Photocatalysis
Terasil blue

**ABSTRACT**

**Introduction:** The present study aimed to investigate the structural, morphological, elemental, optical properties and photocatalytic activity of the bare zinc oxide (ZnO) and Manganese-doped zinc oxide (Mn- ZnO) nanoparticles (NPs) using terasil blue (TB) dye as a model substrate.

**Materials and Methods:** The ZnO and Mn-doped ZnO catalysts were synthesized using the co-precipitation method. The synthesized photocatalysts were characterized by X-ray diffraction (XRD), energy dispersive X-ray (EDX), and scanning electron microscopy (SEM). The band energies were measured using ultraviolet-visible (UV-Vis) spectrophotometry.

**Results:** The results obtained from XRD, EDX, SEM, and UV-Vis analyses demonstrated a successful synthesis of bare and Mn-doped ZnO nanoparticles. The diffraction patterns for the synthesized ZnO and Mn-doped ZnO photocatalyts were matched with that of the standard hexagonal wurtzite structure of the standard ZnO catalyst. The average particle size for the ZnO and Mn-doped ZnO catalysts were found to be 23.46 nm and 24.38 nm, and band gap energies of 3.28eV and 3.09eV, respectively. The photocatalytic performance of the Mn-doped ZnO photocatalyst was optimized using box behnken design of response surface methodology under visible light irradiation. The operational parameters involved TB initial concentration, catalyst dosage, initial pH, and irradiation time. The optimum photodegradation efficiency of TB dye removal was achieved at 96.75% of 15mg/L of TB concentration, 0.1g/L of Mn-doped ZnO, pH = 10, and 160 minutes of irradiation time. Moreover, the photocatalytic degradation of TB over the Mn-doped ZnO nanoparticles followed the pseudo-first-order kinetics model (k = 0.0254 min-1).

**Conclusion:** Finally, the evaluation of various scavengers confirmed that the photogenerated holes and hydroxyl radicals were the major radicals for the TB photodegradation over the Mn-doped ZnO nanoparticle under visible light irradiation.

## 1. Introduction

The discharge of poorly treated disperse dyes enriched with several recalcitrant chemicals and carcinogenic substances into open water is a severe problem for terrestrial and aquatic life[1-3]. Disperse dyes, which are artificial coloring agents designed for hydrophobic surfaces, find extensive application as commercial blends in the coloring of textiles. Terasil blue (TB) dye is at the forefront of dispersed dyes with C I 60767. The TB dye exhibits limited solubility in water, possesses non-ionic characteristics, and can be employed on hydrophobic fibers through an aqueous dispersion[4,5]. While TB dyes are predominantly utilized on polyester, they have also been applied to nylon, cellulose acetate, and acrylic fibers. However, some wet-fastness properties of the TB dye on the substrates are poor[6]. The TB dye substrate usually remains unclear and highly polluted due to the dyeing and dumping of industrial effluents directly into the ecosystem[7].

► *Cite this paper as*: Yusha'u A, Abdulfatah S, Kabo KS, Muhammad A. The Use of Manganese-Tunable *p*-type ZnO Nanoscale for Optimized Photocatalytic Degradation of Terasil Blue from Wastewater. Research in Biotechnology and Environmental Science. 2023; 2(4): 88-101. DOI: 10.58803/rbes.v2i4.32

The removal of TB dye by the classical and conventional methods, such as adsorption, sedimentation, precipitation, and biodegradation, recorded poor success due to the generation of secondary sludge, high costs, and the need for additional planning[8,9]. Gzar and Sabri[10] studied the removal of TB dye from synthetic wastewater using low-cost agro-based adsorbents. The findings indicated that the maximum removal efficiency of TB on canocarpus was 87.5% at 50 rpm mixing speed, pH value 3, mixing time 7 hours, and the sorbent dose of 0.25g. Similarly, Jaeel[11] investigated the adsorption of TB on prosopis farcta, conducting a performance and modeling study. The experimental results demonstrated that the maximum removal efficiency of TB dye over PF reached 85% at a fixed 200 rpm mixing speed, pH value 8, mixing time of 90 minutes, and dose of adsorbent 0.5 g.

Heterogeneous photocatalysis has been recognized as an alternative method for the removal of pollutants, such as TB dye from the aqueous environment[12]. The method, however, involves the use of hole and hydroxyl radicals significantly harvested from the light-excited photoresponsive catalyst[13]. Photoresponsive catalysts are semiconductor substances that alter the rate of chemical reactions in the presence of UV-Vis light irradiation. The common examples of photoresponsive catalysts are $TiO_2$, ZnO, CdO, $ZrO_2$, CdS, ZnS, $WO_3$, $Fe_2O_3$, CdTe, and $SrTiO_2$[14-16]. However, the abovementioned photocatalysts are widely used for the degradation of organic and inorganic pollutants, sensors, purification of air, and purification of soil, degradation of cancers, and microorganisms[17-20]. Zinc oxide photoresponsive is a promising candidate widely used as a photocatalyst for the degradation of both organic and inorganic pollutants from the environment due to its stability, non-toxic, availability, low cost, and environmental friendliness, compared to the other photocatalysts[21-24]. Despite its advantages, ZnO photocatalyst has limitations, including its wide band gap (3.26 eV), which restricts its absorption of ultraviolet (UV) light, and its susceptibility to photocorrosion and electron recombination processes. To overcome these drawbacks, different methods have been employed to modify band gap energy, reduce the rate of electron recombination, and shift the spectral response from UV light to visible light irradiation[25,26]. Transition metal-dopant materials, such as Mn, Fe, Cr, and Cu, have proven effective for this purpose[25,26]. This study chooses manganese (Mn) as the metal of interest for tuning the ZnO photoresponsive catalyst. This selection is based on the ready availability of Mn's d electrons at the t2g level and their easy overlap with the valence band of the ZnO photocatalyst[27-30].

Previously, the photocatalytic activity of Mn-doped ZnO nanoparticles highlighted a significant success[31,32]. Aadnan *et al*. investigated the structural, optical, and photocatalytic properties of Mn-doped ZnO nanoparticles as photocatalyst for azo-dye degradation under visible light. The experimental results revealed that 96% of the azo-dye was degraded[33]. Dhanshree and Elangovan conducted a comprehensive investigation into the synthesis and characterization of ZnO and Mn-doped ZnO nanoparticles, revealing noteworthy spectral responses and experimental results[34]. In a related study, Otadi et al. focused on the synthesis and characterization of Mn-doped ZnO nanoparticles, employing Taguchi experimental design and molecular mechanic simulation for the degradation of pyridine in a batch reactor. Their results indicated a marked improvement in the degradation of pyridine when using Mn-doped ZnO compared to undoped ZnO nanoparticles[35]. Similarly, Khan et al. conducted an investigation on the production, characterization, and assessment of the biological properties of Mn-doped ZnO. The findings revealed that Mn-doped ZnO exhibited more pronounced antibacterial and antioxidant activities compared to the undoped ZnO photocatalyst[36].

Despite the existing body of scientific literature, research on the photocatalytic removal of TB dye over the Mn-doped ZnO nanoparticles from the wastewater is scarce. Therefore, the present study aimed to investigate the structural, morphological, elemental, optical properties and photocatalytic activity of the ZnO and Mn-doped ZnO nanoparticles. The photocatalytic degradation of TB dye over the synthesized Mn-ZnO nanoparticles under visible light irradiation was optimized using the Box-Behnkhen design (BBD) of the response surface methodology (RSM). The independent variables were the TB initial concentration, initial pH, catalyst doses, and irradiation time. In addition, the study also investigated mineralization, kinetics, reusability, and scavenger tests for the photocatalytic degradation of TB over the Mn- ZnO catalyst.

## 2. Materials and Methods

### *2.1 Materials*

The chemicals and reagents utilized in the study were obtained from Sigma-Aldrich (United States of America) and Merck (Germany) and were of analytical grade. These reagents included zinc nitrate [$Zn(NO_3)_2).6H_2O$, 98% purity], manganese nitrate [$Mn(NO_3)_2.4H_2O$, 96% purity], sodium hydroxide [ NaOH, 98% purity], dilute hydrochloric acid [HCl, 98% purity], TB dye (98% purity) and deionized water. The chemical structure of TB is shown in Figure 1.

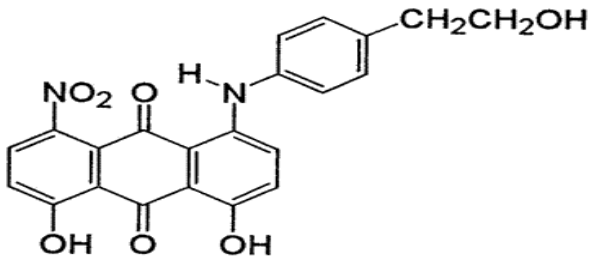


**Figure 1.** Chemical structure of terasil blue dye

### 2.2 Methods

#### 2.2.1 Preparation of solution

Zinc nitrate hexahydrate [$Zn(NO_3)_2).6H_2O$, 0.07M] was prepared by dissolving 7.746g of zinc nitrate in deionized water in a 500 ml volumetric flask, with solution level brought up to the merk, and then stirring for 15 minutes. Next, a 0.07 M solution of manganese nitrate [$Mn(NO_3)_2.4H_2O$] was provided by dissolving 3.465g of manganese nitrate in 200 ml deionized water in a measuring flask. Sodium hydroxide solution (45%) was also prepared in deionized water.

#### 2.2.2. Synthesis of zinc oxide photocatalyst

The process reported by Hamza et al. was adopted and modified to synthesize the bare ZnO nanoparticles[37]. Zinc nitrate (0.07M, 500 ml) was introduced into a 1000 ml beaker and stirred for 35 minutes at room temperature (28℃) using a magnetic stirrer/hot plate at the rate of 2000 rpm. Dilute sodium hydroxide (45%) was added slowly with constant stirring for 60 minutes, and the pH was adjusted to approximately 9.0 using dilute HCl or NaOH. After obtaining the desired pH (9.0), the reaction mixture was heated at 70℃ with continuous stirring for 25 minutes using a magnetic stirrer at 2000 rpm. Subsequently, the mixture was left at room temperature for 2 days to facilitate precipitation, yielding white precipitates in the reaction mixture. To isolate the white ppts, the reaction mixture underwent filtration and was washed three times with 30 ml of deionized water to eliminate impurities.. Thereafter, the ppts were filtered and oven-dried at 110℃ for 60 minutes. The dried ppts were milled using a pestle and mortar, and then the powder was heated in the oven for 20 minutes at 110℃ to remove any absorbed moisture. Then, calcination of the white powder at 300℃ for 2 hours in a muffle furnace. This resulted in a white, fine powder that was cool to room temperature and thus leveled as bare ZnO nanoparticles.

#### 2.2.3. Synthesis of mn-doped zinc oxide photocatalyst

To perfom the synthesis Mn-doped ZnO nanoparticles, the reserachers followed a previously used method[36]. The process involved mixing manganese nitrate and zinc nitrate solutions, and diluting sodium hydroxide (45%) to obtain the pH of 9.0. In a 1000 ml beaker, 500 ml of 0.07M zinc nitrate was gradually added to 50 ml of 0.07M manganese nitrate with continuous stirring. The reaction mixture was stirred for 25 minutes using a magnetic stirrer at the rate of 2000 rpm. In the next step, dilute sodium hydroxide was added from the burette to the reaction mixture at a 2 ml/min flow rate to reach a pH of approximately 9.0. The mixture was gently stirred in a magnetic stirrer at 1000 rpm during the pH adjustment. Following the pH adjustment, the solution underwent additional stirring with a magnetic stirrer at the rate of 1500 rpm for 60 minutes. Subsequently, the reaction mixture was heated at 70℃ for 25 minutes, and placed at room temperature for 2 days for precipitation. This process formed brown-colored precipitates in the reaction mixture. To isolate the precipitates, the reaction mixture was filtered and washed thrice with deionized water and then washed three times with 30 ml of deionized water to dimnish impurities. Later, the precipitates were over-dried at 110℃ for an hour and milled in a pestle and mortar. The resulting brown powdered nanoparticles underwent heating for 20 minutes at 110℃ to eliminate any trace of absorbed moisture. This process yielded brown and fine powdered particles that were characterized as Mn-doped ZnO nanoparticles.

### 2.3. Photocatalysts characterization techniques

To ascertain the crystal structure, lattice strain, crystallite size, lattice phase, chemical composition, and purity of the as-synthesized catalysts, the powder X-ray diffraction (PXRD) analysis was done using Philps X pert Pro diffractometer instrument operated with a $CuK_\alpha$ radiation (λ= 1.54468 Å) at 40 kV, 30 mA. Measurements were scanned for diffraction angle (2ɵ) ranging from 20-90˚ with a step size of 0.02˚ and time per step of a second. The lattice parameters consist the spacing distance between the adjacent planes in the miller indices $d_{hkl}$, lattice constant a, b, and c (Equations 1-4).

$$a = b = \frac{\lambda}{\sqrt{3}\sin\theta 100} \quad (1)$$

$$c = \frac{\lambda}{\sin\theta 001} \quad (2)$$

$$D = \frac{k\lambda}{\beta\cos\theta} \quad (3)$$

$$SSA = \frac{6000}{D\times\rho} \quad (4)$$

### 2.4. Surface area of the photoresponsive catalysts

The XRD raw data were used to determine the synthesized photocatalyst's surface area (SA). The SA for the bare ZnO photocatalyst was measured using Equations 5 and 6[34].

$$SSA = \frac{SA}{V\times\rho} \quad (5)$$

$$S.A = SSA \times V \times \rho \quad (6)$$

### 2.5. Band gap measurement

The band gap energy ($E_g$) values for the ZnO photocatalyst were determined by analyzing the electronic data recorded for the wavelength range of 200-800 nm on the Lambda 35 Perkin Elmer UV-Visible spectrophotometer. The $E_g$ values for the synthesized catalyst were calculated using the Schuster-Kubelka-Munk relation (Equation 7)[39].

$$(\alpha h\nu)^{\frac{1}{n}} = K(h\nu - E_g) \quad (7)$$

### 2.6. Photodegradation experiments

Photocatalytic performances of the ZnO and Mn-doped ZnO catalysts were studied for TB removal. All experiments were done in a 30 cm long, 1 Liter capacity, round bottom batch photoreactor which was maintained at 298K. The visible light source was a 300W Xenon lamp emitting at 400 nm. This lamp was jacketed in cylindrical quartz glass, dipping down the photoreactor bottom[38].

Typically, 500 ml aqueous solution of the desired amount of TB (10-30mg/L) and Mn-doped ZnO photocatalyst (0.01-0.06g) was added to the photoreactor, and the pH of the suspension was adjusted using 45% NaOH and HCl. This mixture was magnetically stirred for 25 minutes in the dark to establish adsorption equilibrium and then exposed to irradiation under continuous stirring at room temperature (25°C) for 180 minutes. At an interval of 20 minutes, an aliquot of 5ml was taken and filtered using a 0.45 µm cellulose nitrate filter and analyzed for residual concentration of TB at 671nm using a T60 UV-Vis spectrophotometer. The percent photodegradation efficiency (D%) was estimated using Equation 8.

$$D\% = 1 - \frac{[TB]_t}{[TB]_0} \times 100 \quad (8)$$

### 2. 7. Control experiments

Systematic control experiments for the photocatalytic TB degradation over the bare ZnO and Mn-doped ZnO catalysts under ultraviolet (UV, 96W halogen lamp) irradiation and natural sunlight illumination at optimal reaction conditions (15.00 mg/L of initial concentration, 0.05 g/L of catalysts, initial pH of 8.00, and irradiation time of 160 minutes) was conducted and compared with the photocatalysis of TB using Mn-doped ZnO photocatalyst under visible (300W Xenon lamp emitting at 400 nm) light irradiation. The power intensity of sunlight was measured by solarimeter (SL-200-KIMO) every half-hour and found to be 700Wm$^{-2}$ (the experiments were carried out in January 2023). The percentage photodegradation efficiencies were estimated using Equation 8.

### 2. 8. Box-Benhken experimental design

The experimental design and statistical analysis were performed using the BBD of RSM because its uniqueness in generating a higher-order surface response. An experimental design was conducted at three-level-four-variable BBD. These independent variables are the initial TB concentration (A), catalyst loading (B), initial pH (C), and irradiation time (D) operated at three levels (low, central, high) coded -1, 0, and +1 (Table 1). Other variables, including light intensity, delivery volume, agitation speed, and oxygen pressure, were maintained constant. 29 experiments (N) were done using the formula $N = 2^n + 2n + 5$. Where n is the number of variables. The % D obtained from these experiments was processed using the upgraded Design Expert software DX 13.0 to get the predicted responses, response surface, and regression model for the TB degradation.

### 2.9. Kinetics and mineralization profile

A series of experiments were performed at the optimal operating conditions acquired from the response surface methodology. The data obtained was tested using the integrated rate equations (Eq. 9-12) for pseudo-zero order, pseudo-first-order, pseudo-second order kinetics model, and half-life for pseudo-first-order scheme.

$$\frac{[TB.]_0}{[TB.]_t} = -k\,t \quad (9)$$

$$\ln\frac{[TB.]_0}{[TB.]_t} = k_{app}\,t \quad (10)$$

$$\frac{1}{[TB.]_t} - \frac{1}{[TB.]_0} = k\,t \quad (11) \text{ and}$$

$$t_{½} = \frac{0.6988}{k} \quad (12)$$

Where, $[TB.]_0$ and $[TB.]_t$ define the initial and final concentration of TB, t serves as the irradiation time, $k$ and $k_{app}$ are the rate constant and apparent rate constant, respectively, and $t_{½}$ denotes the half-life for pseudo-first-order reactions. The basic kinetic parameter ($k$) was calculated from the plot of $\frac{[TB.]_0}{[TB.]_t}$ against t for pseudo-zero order kinetics. Similarly, a plot of $\ln\frac{[TB.]_0}{[TB.]_t}$ versus t gives a linear graph that passes through the origin and the apparent rate constant, $k_{app}$ (min$^{-1}$) was estimated from the slope. While the plot of $\frac{1}{[TB.]_t}$ against t also gave a linear graph passing through the intercept in which the TB initial concentration was calculated from the intersection and rate constant (k) from the slope. The half-life for the photocatalytic degradation of TB over the synthesized photocatalysts was calculated at optimal conditions.

The progress of the mineralization process was monitored by measuring total organic carbon (TOC) using a Shimadzu 00087 TOC analyzer. The extent of mineralization of TB dye was calculated using Eq. 13.

**Table 1.** The level factorial Box-Benhken design

| Variable | Notation | Levels (Codes) | | |
|---|---|---|---|---|
| **Initial TB concentration (mg/L)** | A | 10(-1) | 15(0) | 20(+1) |
| **Catalyst loading (g/L)** | B | 0.01(-1) | 0.05(0) | 0.10(+1) |
| **Initial pH** | C | 4(-1) | 8(0) | 12(+1) |
| **Irradiation time (min)** | D | 20(-1) | 80(0) | 180(+1) |

TB: Terasil blue

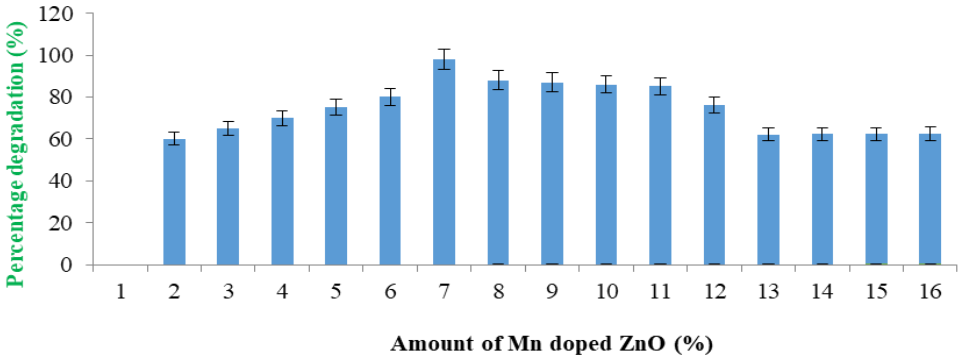


**Figure 2.** Activity of different amounts of manganese doses in the degradation of TB

$$\% \text{ mineralization} = 1 - \frac{[TOC]_t}{[TOC]_0} \times 100 \qquad (13)$$

$[TOC]_0$ is the total organic carbon before mineralization and $[TOC]_t$ is the total organic carbon at a given time t.

### *2.10. Radical scavenger experiments*

The primary reactive radicals and holes were detected through radical scavenging experiments to investigate the significant role of reactive radicals generated during the photocatalytic removal of TB over Mn-doped ZnO nanoparticles. During the photocatalytic process, the holes ($h^+$), hydroxyl radical (• OH), and superoxide radical ($\bullet O^-_2$) are trapped by adding ammonium oxalate (AO), ($h^+$ scavenger), *t*-butanol ((• OH scavenger), and *p*-benzoquinone (($\bullet O^-_2$ scavenger) into the reaction solution respectively. Typically, 10.00mg of Mn-ZnO and 10.00mM of radical scavengers were introduced into 10.00 mg/L of TB solution. Then, the suspension was irradiated using the 300W Xenon lamp emitting at 400nm simultaneously. Finally, the TB photodegradation efficiencies were calculated using Eq. (8).

## 3. Results and Discussion

### *3.1. Preliminary studies*

The photoactivity of different amounts of manganese dopant in removing TB dye was monitored using 15.00 $mgL^{-1}$ solution of TB, 0.05$gL^{-1}$ ZnO catalysts with Mn content in the 2 to 16 % (Figure 2). The observed trend revealed the relationship between the photocatalytic degradation efficiency of TB and the carbon content, indicating an increase from 2% to 7%. However, beyond 7% manganese, there was a consistent decline in degradation efficiency. Thus, 7 % Mn-doped ZnO was found to be the optimal (98%) amount of dopant when compared to the rest of the Mn-doped ZnO photocatalysts. The enhanced photocatalytic activity of the 7 wt% Mn-doped ZnO may be attributed to the creation of just enough shallow trapping sites for the charge carriers by the presence of Mn, which causes a difference in the surface arrival time of electron and hole pairs and prevents recombination[40].

### *3.2. Spectral results*

#### *3.2.1. Structural properties*

Figure 3 displays the powder X-ray diffraction patterns for the U-doped ZnO and Mn-doped ZnO catalysts. As indicated, the reflection peaks at 2θ values of 31.8˚,34.4˚, 36.3˚, 47.6˚, 56.7˚, 62.9˚, 66.5˚, 68.0˚ and 69.1˚ corresponded to the structural miller indices (100), (002), (101), (102), (110), (103), (200), (112), and (201) of U- ZnO catalyst. Similarly, the diffraction peaks observed at 2θ = 31.7˚. 34.4˚, 36.2˚, 47.6˚, 56.6˚, 62.8˚, 66.4˚, 67.9˚, and 69.0˚ corresponded to the (100), (002), (101), (102), (110),

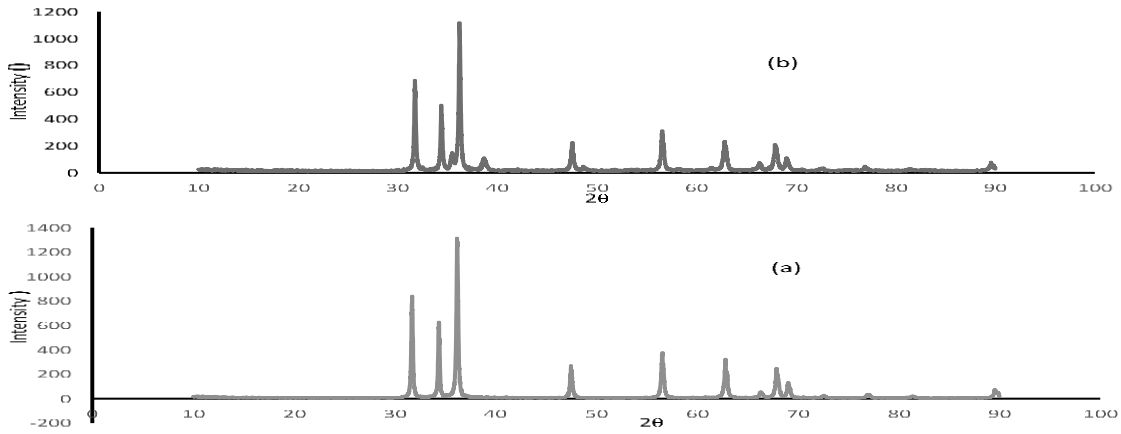


**Figure 3.** The X-ray diffraction patterns of photocatalysts. a: Undoped ZnO, b: Mn-doped ZnO

**Table 2.** The lattice parameters and crystal structure of undoped and Mn-doped ZnO catalysts

| Photoresponsive Catalyst | $d_{100}$(Å) | Lattice parameters in (Å) | | Crystal structure | Volume of a unit cell (Å) | Unit cells per particle |
|---|---|---|---|---|---|---|
| | | a = b | c | | | |
| ZnO | 2.9216 | 3.2476 | 5.2031 | Hexagonal wurtzite | 47.4939 | 1.2868 |
| Mn-doped ZnO | 2.9136 | 3.2495 | 5.2040 | Hexagonal wurtzite | 47.5869 | 1.9721 |

ZnO: Zinc oxide, Mn-doped ZnO: Manganese-doped zinc oxide

(103), (200), (112), and (201) reflection planes of the Mn-doped ZnO nanoparticles (Figure 3b). The absence of impurity peaks is a primary manifestation of a single phase, low content of accommodated dopant, and high purity of the synthesized photocatalysts[41].

The obtained XRD patterns for the ZnO and the Mn-doped ZnO matched the standard hexagonal wurtzite structure of ZnO catalyst (JCPDS 01-080-9087). As can be seen in Table 2, The unit cell parameters calculated based on ZnO lattice planes (101) and (102) aligned with the standard lattice parameters (a = 3.2465Å and c = 5.2030Å; JCPDS Card no; 070-7036) and (a = 3.2494Å and c = 5.2038Å; JCPDS Card no; 01-087-7523, respectively). The values calculated showed slight increases in the unit cell parameters, including the spacing distance and unit cell volume (Table 2).

The high crystallinity of the as-prepared ZnO powders is indicated by the outstanding sharpness of diffraction peaks[42]. Upon doping, the specific surface area of the Mn-doped ZnO increased from 45.78 to 58.27 ($m^2g^{-1}$) while the XRD-based particle size slightly increased from 23.46 to 24.38 nm (Table 3). These findings are in line with the previous report[32]. Moreover, an increase in the surface area of Mn-doped ZnO photocatalysts has usually been linked to enhanced interfacial reactions[43].

### *3.2.2. Morphological properties*

The surface morphology of the as-prepared bare ZnO and Mn-doped ZnO is shown in Figure 4. The aggregation of particles is seen in the U- ZnO nanoparticles (Figure 4a), and agglomeration of the particles was pronounced for the Mn-doped ZnO nanoparticles (Figure 4b). This might be due to the addition of dopant (Mn) during the synthesis[44]. These results are consistent with the previous report[45]. Therefore, Figure 4 reveals the surface morphology of synthesized photocatalysts.

### *3.2.3 Elemental properties*

The presence of the Mn atom with Zn and O atoms in the nanoparticles is substantiated by EDX analysis. Figure 5 illustrates the EDX spectra of bare ZnO and 7% Mn-doped ZnO nanoparticles (the optimal catalyst). Figure 5a demonstrates that the spectra consist of Zinc (Zn) and oxygen (O) atoms only, while Figure 5b shows the presence of Zinc (Zn), oxygen (O) and manganese (Mn) atoms. These results provide concrete evidence of the successful synthesis of both U-ZnO and Mn-doped ZnO nanoparticles, emphasizing the high purity of the sample synthesized. These findings are consistent with the previous report[36,46].

The weight and atomic percent composition of Zn and O atoms for (a) U-ZnO and Zn, O, and Mn atoms in the Mn-doped ZnO are shown in Table 4. Despite ZnO generally being considered an n-type semiconductor with predominant defects like interstitial zinc and oxygen vacancies, the current results showed zinc and oxygen excess deficiency. This implies the existence of interstitial oxygen and the less observed *p*-type semiconducting ZnO nanoparticles[47].

**Table 3.** The size, surface area, and band gap of the ZnO Mn-doped ZnO nanoparticles

| Photocatalyst | D(nm) | Specific surface area ($m^2g^{-1}$) | Band gap (eV) |
|---|---|---|---|
| U- ZnO | 23.46 | 45.78 | 3.28 |
| Mn-doped ZnO | 24.38 | 58.27 | 3.09 |

D: Average crystallite size

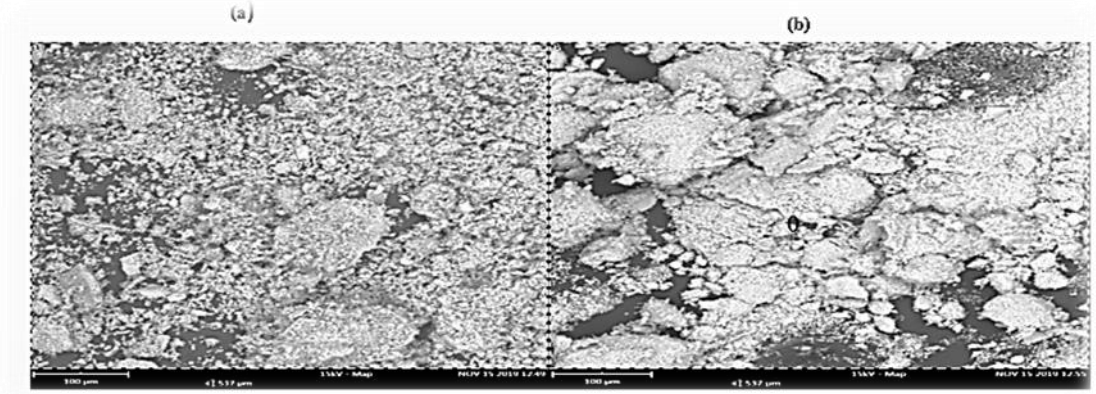


**Figure 4.** The SEM Micrographs of (a) Undoped ZnO and (b) Mn-doped ZnO nanoparticles.

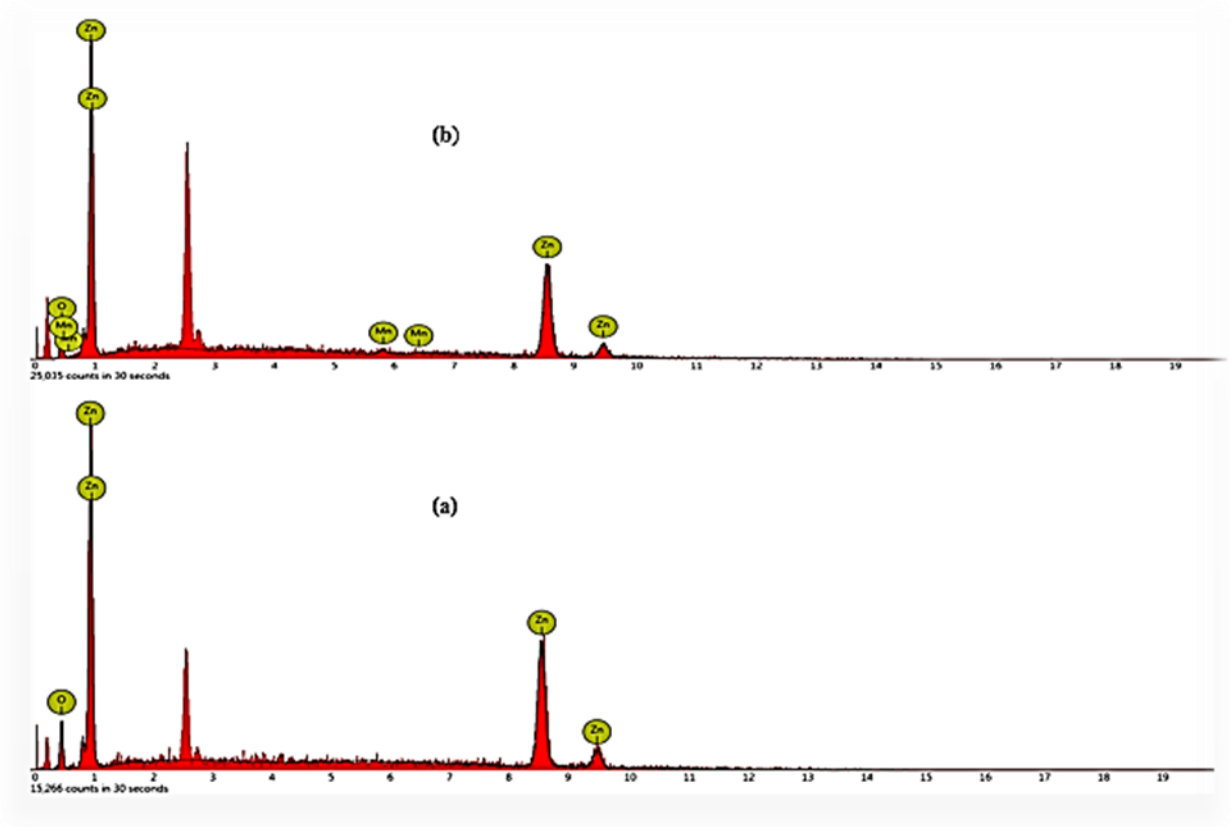


**Figure 5.** The EDX spectra (a) undoped ZnO and (b) Mn-doped ZnO nanoparticles

**Table 4.** Weight and Atomic percentage of the constituents of undoped and Mn-doped ZnO nanoparticles

| Element | U- ZnO nanoparticles | | Mn-doped ZnO nanoparticles | |
|---|---|---|---|---|
| | Wt% | At% | Wt% | At% |
| Mn K | - | - | 4.94 | 3.80 |
| O K | 18.99 | 50.51 | 23.03 | 53.56 |
| Zn L | 81.01 | 50.49 | 72.03 | 42.64 |
| Total | 100 % | | 100 % | |

U-ZnO: Undoped zinc oxide, Wt%: Weight percentage, At%: Atomic percentage, Mn-doped ZnO: Manganese doped zinc oxide, Mn K: Manganese K-shell, O K: Oxygen K-shell, Zn L: Zinc L-shell

### *3.2.4 Optical properties*

The band gap energies of the obtained ZnO nanoparticles were measured from the absorption data using Kubelka-Munk's intercept of the plot of $(\alpha h\upsilon)^2$ against hv (Figure 6). The figure shows linearity in the vicinity of the band gap region for both the Mn-doped ZnO and that of the bare ZnO, revealing that the Mn-doping did not change the direct electron transition characteristics of the ZnO[36]. The band gap energy values for the undoped and Mn-doped ZnO photocatalysts were 3.28eV and 3.09 eV, respectively, confirming the ability of the former to absorb more visible light relatively. In other words, Mn doping reduces the band gap energy of the bared ZnO catalyst due to decreased particle size and adsorption capacity between the Mn-doped ZnO and pollutant, which further contributes to the charge-transfer process easily[48]. The observed ease of charge transitions suggests that Mn-doped ZnO exhibits higher conductivity compared to bare ZnO catalyst. Consequently, Mn-doped ZnO nanoparticles demonstrate excellent conductivity, making them suitable for applications as electrophotocatalysts in photoelectrochemical reactions[49].

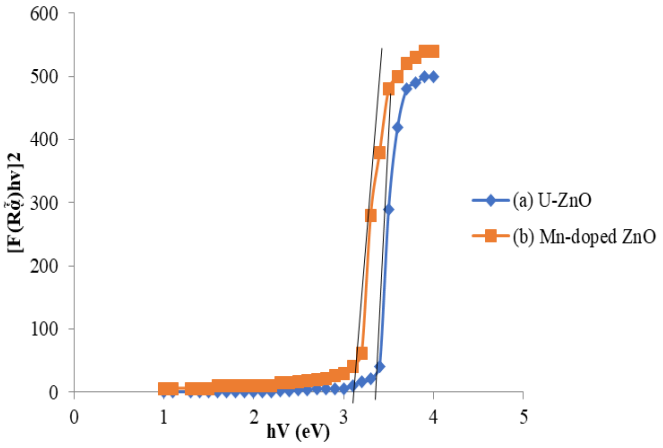


**Figure 6.** Band gap plots for the ZnO powders. U-ZnO (a) Mn-doped ZnO nanoparticles (b)

**Table 5.** Results of Box-Behnkhen design with experimental and predicted degradation efficiencies

| Run | Experimental efficiencies ($\%D_{exp}$) | Predicted efficiencies ($\%D_{pred}$) |
|---|---|---|
| 1 | 67.00 | 71.88 |
| 2 | 89.00 | 87.04 |
| 3 | 87.00 | 93.54 |
| 4 | 78.00 | 77.71 |
| 5 | 73.00 | 87.71 |
| 6 | 97.00 | 89.21 |
| 7 | 79.00 | 91.38 |
| 8 | 98.00 | 87.88 |
| 9 | 92.00 | 94.63 |
| 10 | 78.00 | 82.79 |
| 11 | 87.00 | 84.29 |
| 12 | 96.00 | 95.46 |
| 13 | 96.00 | 90.96 |
| 14 | 91.00 | 74.63 |
| 15 | 49.00 | 67.46 |
| 16 | 96.75 | 96.65 |
| 17 | 94.00 | 88.83 |
| 18 | 80.00 | 79.50 |
| 19 | 85.00 | 78.83 |
| 20 | 89.00 | 87.50 |
| 21 | 93.00 | 81.00 |
| 22 | 96.00 | 93.67 |
| 23 | 93.00 | 88.67 |
| 24 | 83.00 | 88.33 |
| 25 | 94.00 | 88.40 |
| 26 | 90.40 | 88.40 |
| 27 | 91.00 | 88.40 |
| 28 | 80.00 | 88.40 |
| 29 | 87.00 | 88.40 |

### *3.3. Experimental results and process optimization*

#### *3.3.1 Statistical analysis*

A total of 29 runs of BBD were conducted. The TB degradation efficiencies of the various photoexperiments ($\%D_{exp}$) and the corresponding statistically predicted values (($\%D_{pred}$) are shown in Table 5. The experimental optimum photoremoval efficiency (96.75%) was achieved at A-initial concentration of TB (15.00 $mgL^{-1}$), B-catalyst doses (0.1$gL^{-1}$), C-pH (10), and D-irradiation time (160 minutes).

Table 5 demonstrates that the experimental and predicted photodegradation efficiencies are in good correlation, as attested by the linear correlation of normal probabilities plot of residuals (Figure 7). Most of the normal probability plot points lied roughly in a straight line.

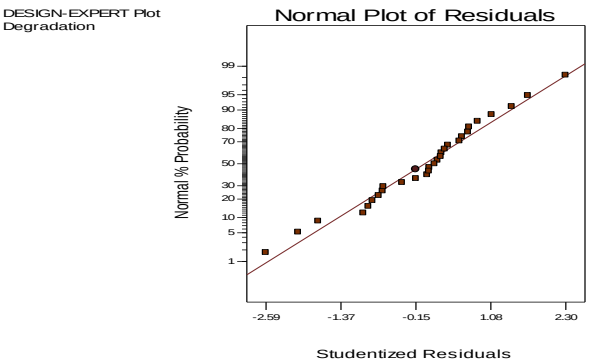


**Figure 7.** Linear normal plot of residual

The removal model was of a reduced quadratic type, as indicated by Equation 14, due to the absence of support from the irradiation time term (D), cross terms (AB, AC, AD, BC, BD, CD), and the square term ($D^2$) in the model hierarchy.

$$D\% = +80.73+1.28A-1.98B+0.98C+2.22A^2-0.20B^2-0.98C^2 \quad (14)$$

Table 6 shows the results of ANOVA for the reduced quadratic model applicable to this study. As can be seen, the F-values of the model and the model terms A, B, C, $A^2$, $B^2$, and $C^2$ were > 4, indicating low chances of noise and confirming the significance of the quadratic model. This is further corroborated by the values of Prob >F, which are all < 0.05 less. The quality of the developed model was high, given that $R^2$ = 0.9815. This implies that the independent variables within the studied range explained 96.75 % of the variations for the removal of TB dye. The lack of fit value of 0.62 was insignificant compared to the pure error with the p-value of 0.7621 > 0.05, indicating the model predictability. Meanwhile, the small p-value (below 0.0001) confirmed the significance of the model term. Therefore, the significant terms among the tested process parameters were solution pH > TB concentration > second order of solution pH > second order of Mn-ZnO photocatalyst dosage > Mn-ZnO photocalysts dosage > second order of TB concentration. Other model terms were insignificant, as their p-values were above 0.1000.

As indicated in Table 7, the coefficient of variance (CV = 1.14) was low, indicating high precision and good reliability of the experimental values. Adequate precision

**Table 6.** Analysis of variance for the quadratic model

| Source | Sum of square | df | Mean Square | F value | P value | Remarks |
|---|---|---|---|---|---|---|
| Model | 6546.54 | 6 | 6543.00 | 13.89 | 0.0001 | significance |
| A | 5671.32 | 1 | 5671.32 | 88.65 | <0.0001 | |
| B | 345.34 | 1 | 345.34 | 6.75 | 0.0012 | |
| C | 145.21 | 1 | 145.21 | 7.11 | 0.0014 | |
| $A^2$ | 134.21 | 1 | 134.21 | 12.22 | 0.0073 | |
| $B^2$ | 543.11 | 1 | 543.11 | 14.62 | 0.0092 | |
| $C^2$ | 1145.34 | 1 | 1145.34 | 13.11 | 0.9870 | |
| Residual | 1237.32 | 22 | 58.12 | | | |
| Lack of fit | 876.76 | 18 | 77.78 | 0.62 | 0.7621 | not significant |
| Pure Error | 345.11 | 4 | 72.14 | | | |
| Cor. Total | 897.58 | 28 | | | | |

df: Degree of freedom

**Table 7.** Analysis of variance results for the quadratic model

| Parameter | Value |
|---|---|
| Standard deviation | 3.01 |
| Mean | 82.72 |
| Coefficient of variance (CV,%) | 1.14 |
| Coefficient of determination ($R^2$) | 0.979 |
| Adjusted $R^2$ | 0.969 |
| Predicted $R^2$ | 0.798 |
| Adequate precision | 33.17 |

measure of 33.17, which was well above 4, revealed an adequate signal. The regression model demonstrated a good relationship between independent variables, as both $R^2$ (0.988) was close to 1. The p values of the major parameters (A and C) influencing the percentage removal of TB were significant ($p < 0.05$). Similarly, the quadratic terms ($A^2$ and $B^2$) had a probability of less than 0.05, revealing a significant contribution to TB degradation.

In order to validate the reduced quadratic model obtained in this study, individual runs were conducted at low, middle, and high levels, and the obtained results were compared to the predicted values (Table 8). The experimental results were very close to the predicted values (96.66 %), confirming the reliability of the BBD.

### *3.3.2. 3D Response surface plot analysis*

Figure 8 indicates the response surface plots showing the effect of operating parameters. Figure 8a indicates the three-dimensional response surface of the influence of Mn-doped ZnO nanoparticles and initial TB concentration at constant initial pH and irradiation time. The degradation percentage enhanced proportionally with the enhancement of Mn-doped ZnO catalyst due to enhancement in the generation of hydroxyl radicals. Higher catalyst loading was antagonistic to the degradation process due to the reduced catalyst surface area available for light absorption and TB adsorption. Figure 8b shows the effect of TB initial concentration and initial pH solution in removing TB dye. However, the degradation efficiency decreased with enhancing TB concentration ascribed to the interception of the photon before they reach the surface of the Mn-ZnO photocatalyst. Furthermore, the Columbia repulsion between the negatively charged Mn-doped ZnO photocatalyst surface and hydroxyl anions at highly alkaline conditions reduced the TB removal rate by suppressing the generation of hydroxyl radicals. Figure 8c demonstrates the interaction between the initial TB concentration and irradiation time at constant pH and catalyst doses. However, the removal efficiency increased with increasing irradiation time and decreasing TB initial concentration. On the other hand, the percentage photo removal decreased with decreasing irradiation time and increasing TB initial concentration.

### *3.4 Evaluation of photocatalytic activity of optimized Mn-ZnO nanoparticle*

In order to determine the implication of the photocatalytic degradation of TB over the optimized Mn-ZnO nanoparticles under visible light irradiation, two control experiments were conducted under two different experimental conditions. The first was performed under UV; the second was under natural sunlight at optimal reaction variables (15.00 mg/L TB initial concentration, 0.1 g/L of Mn-ZnO, initial pH of 10, and irradiation time of 160 minutes). The results are illustrated in Figures 9-11. From Figure 9, the photocatalytic removal of TB over bare ZnO and Mn-doped ZnO catalysts under visible light resulted in percentage removals of 96.88% and 81.00%, respectively. This clear disparity indicates that the Mn-doped ZnO photocatalyst, as synthesized, exhibits superior photodegradation efficiency for TB removal compared to the pure ZnO photocatalyst. The heightened photocatalytic activity of Mn-doped ZnO can be attributed to potential penetration and enhanced stimulation of nanoparticles by visible light[29,30].

**Table 8.** Validation data for the analysis of variance

| Run | Initial terasil blue concentration (mg/L) | Catalyst loading ($gL^{-1}$) | Initial pH | Experimental efficiency (%) | Predicted efficiency (%) |
|---|---|---|---|---|---|
| 1 | 10.00 | 0.01 | 4.00 | 77.46 ± 0.45 | 77.01 |
| 2 | 15.00 | 0.05 | 8.00 | 96.46 ± 0.03 | 96.66 |
| 3 | 20.00 | 0.1 | 12.00 | 71.69 ± 0.35 | 71.34 |

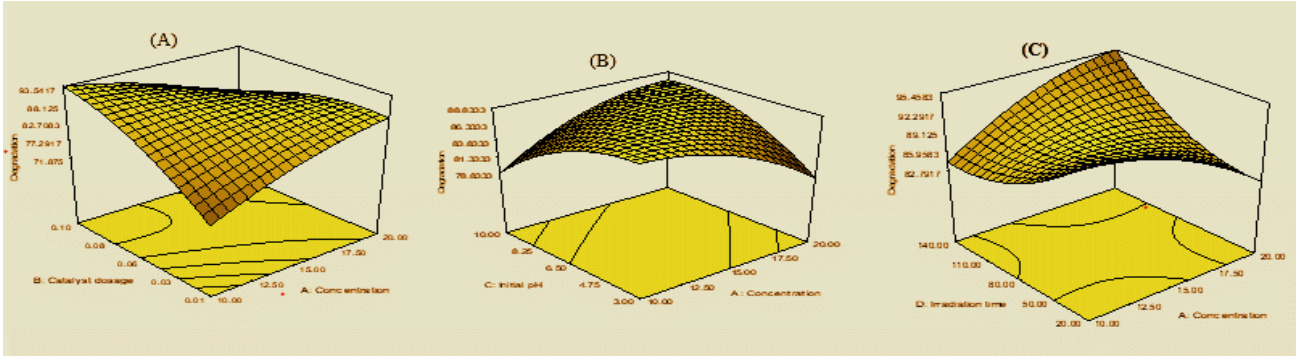


**Figure 8.** Response surface plots showing the interaction of initial terasil blue concentration with (a) catalyst dosage (b) initial pH (c) Irradiation time

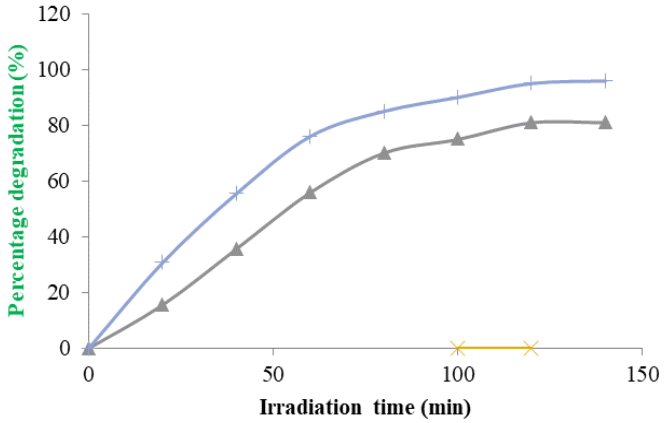


**Figure 9.** Effect of irradiation time on the photocatalytic degradation of terasil blue under visible light irradiation ZnO (a) Mn-doped ZnO (b)

Concurrently, the percentage removal of TB by photocatalysis over the pure ZnO and Mn-doped ZnO nanoparticles under UV light was 92.50 % and 80.00 %, respectively (Figure 10). This indicates that the as-synthesized ZnO photocatalyst has a better photodegradation efficiency for removing TB than the Mn-doped ZnO catalyst. The high photocatalytic activity of the ZnO can be attributed to its wide band gap, possible penetration, and high stimulation of nanoparticles by UV light[29, 53].

Similarly, TB removal rates of by photocatalysis over the undoped ZnO and Mn-doped ZnO nanoparticles under natural light were 86.90 % and 74.50 %, respectively, indicating better photoeffiency of the synthesized ZnO photocatalyst for TB removal (Figure 11). The high photocatalytic activity of the ZnO can be attributed to its wide band gap, possible penetration, and high stimulation of nanoparticles by the natural sunlight[53]

The results presented in Figures 9, 10, and 11, depicting the photocatalytic degradation of TB dye over synthesized ZnO and Mn-doped ZnO nanoparticles under various experimental conditions, clearly elucidate that the TB removal rate of 96.88% achieved over the optimized Mn-doped ZnO under visible light irradiation is significantly superior to the degradation of TB over ZnO. This is due to the low band gap and reduced rate of the

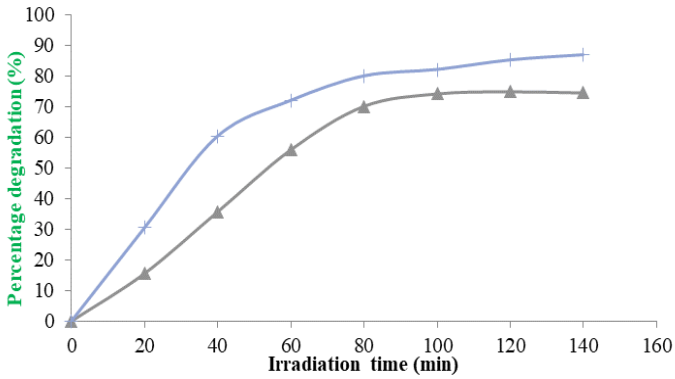


**Figure 10**. Effect of irradiation time on the photocatalytic degradation of terasil blue under UV light irradiation Mn- ZnO (a) ZnO(b)

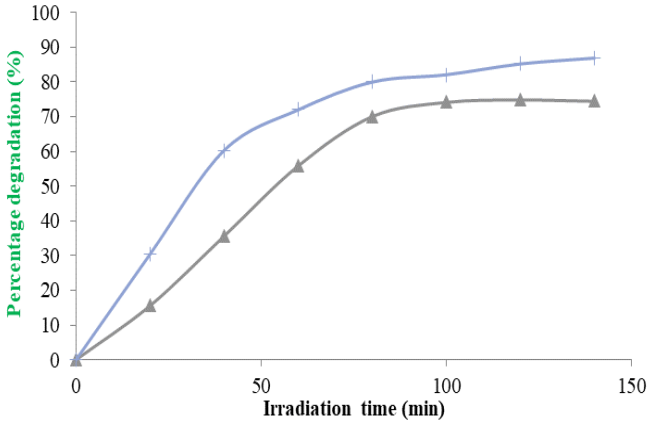


**Figure 11.** Effect of irradiation time on the photocatalytic degradation of terasil blue under natural sunlight irradiation Mn- ZnO (a) ZnO(b)

electron recombination process. Thus, the optimized Mn-doped ZnO nanoparticles could be used for the treatment of wastewater as well as other pollutants such as pesticides, herbicides, microorganisms (bacteria, viruses), purification of air, self-cleaning, treatment of trace metals and artificial photosynthesis[25, 35, 36]. Furthermore, the present study can also be applied in the textiles, papers, ceramics, plastics, rubbers, and pharmaceutical industries to treat their effluents[29,30, 53]. In addition, the optimized Mn-doped ZnO catalyst can also be used in other fields of science and technology for different purposes[25]. For instance, in electrochemistry, the Mn-ZnO catalyst could be used as a good conductor because of the transition of electrons between the valence band and conduction band[53]. In biotechnology, the optimized Mn-ZnO catalyst could produce biofuel and biodiel[29]. Similarly, in health, this study can be used to treat cancer cells from the patient[25,36]. Thus, the optimized Mn-doped ZnO catalyst could be practically applied to treat wastewater and other relevant areas, as stated before.

### *3.5. Reusability study*

To consider the reusability of the Mn-doped ZnO nanoparticles, a systematic experiment was done at the optimum conditions of the photocatalytic removal of TB over the Mn-doped ZnO. Residual catalyst from the degradation experiment was filtered, washed, dried, and then recycled in the fresh experiment (Figure 12).

The observations from Figure 12 reveal a steady decrease in the degradation of TB during the first and second cycles, but from cycles 3 to 7, the degradation remains consistent. This pattern illustrates the stability and effectiveness of the Mn-doped ZnO nanoparticles in TB degradation.

### *3.6. Photocatalytic mechanism*

During TB photocatalytic removal of dye over the Mn-

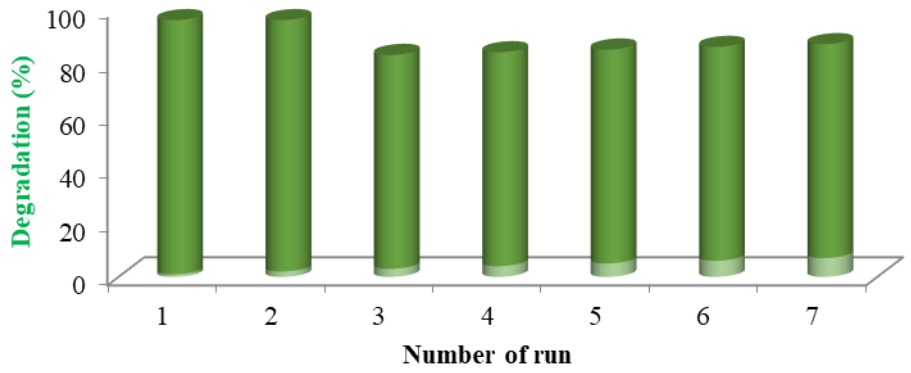


**Figure 12.** Reusability of Mn-doped ZnO in the degradation of terasil blue dye

doped ZnO nanoparticles, the $h^+$, • OH, and • $O_2^-$ are eliminated by adding AO ($h^+$ scavenger)[50], *t*-BuOH (• OH scavenger)[51], and *p*-BQ (• $O_2^-$ scavenger)[52] into the reaction solution respectively and the result is presented in Figure 13.

Figure 10 indicate that adding *p*-BuOH and AO could slightly change TB photocatalytic removal, while a significant change was observed with the addition of *p*-BQ scavenger. These show that the decrease of the photocatalytic removal in the presence of scavengers presents benzo-quinonine > ammonium oxalate> tertiary-butanol. So, the hydroxyl radicals (• OH) are the main reactive species during the photocatalytic removal of TB under visible light irradiation.

### *3.7. Mineralization and kinetics study*

Mineralization is among the most desirable parameters in the degradation of TB dye over the Mn-doped ZnO nanoparticles. In the current study, mineralization was monitored based on total organic carbon (TOC) measurement (Figure 14).

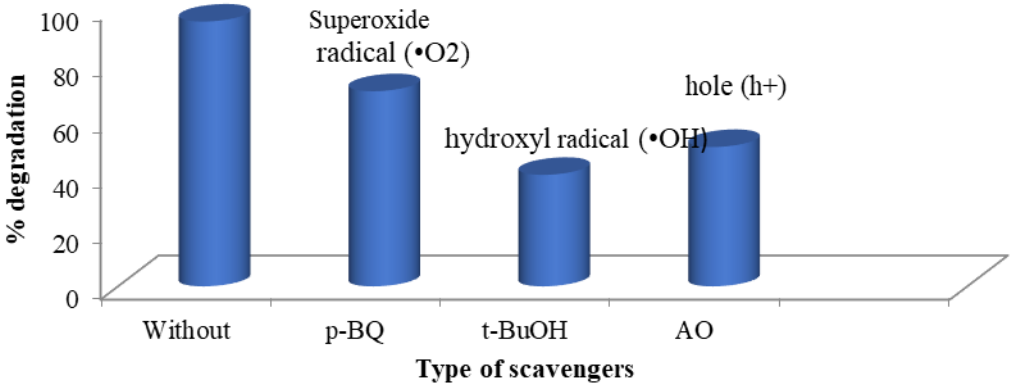


**Figure 13.** Degradation efficiency of terasil blue in the absence and presence of scavengers

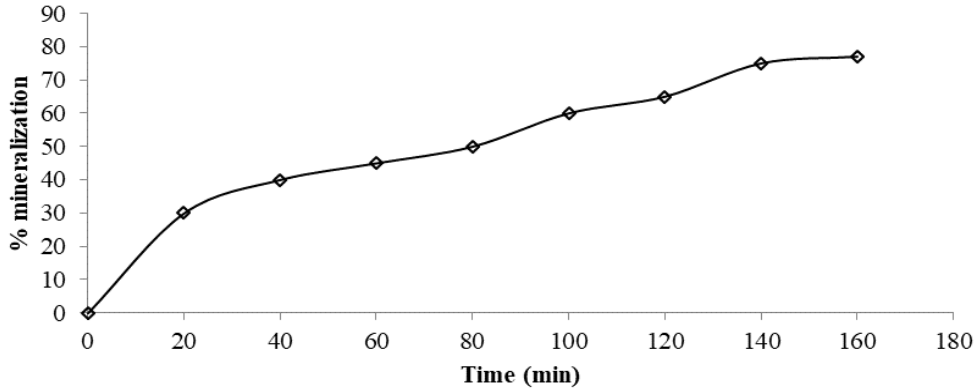


**Figure 14.** Variation of terasil blue mineralization with time at optimized conditions

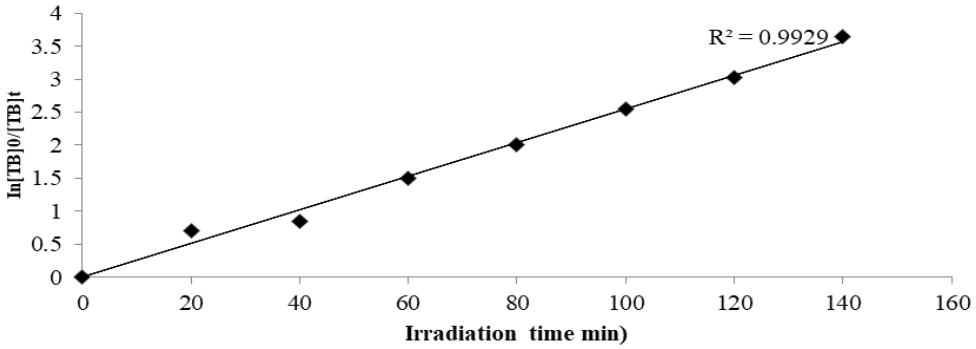


**Figure 15.** Pseudo-first-order plot of degradation of terasil blue over the Mn-doped ZnO nanoparticles

**Table 9.** Kinetic parameters for the degradation of terasil blue ver the Mn-doped ZnO nanoparticles

| S/N | Schemes | Apparent rate constant ($k_{app}$), $min^{-1}$ | Regression model ($R^2$) value | Half-life ($t_{1/2}$) $min^{-1}$ |
|---|---|---|---|---|
| 1.0 | Pseudo-zero-order | 0.0236 | 0.9239 | 1.569 |
| 2.0 | Pseudo-first-order | 0.0254 | 0.9929 | 1.658 |
| 3.0 | Pseudo-second-order | 0.0124 | 0.8999 | 1.763 |

S/N: Serial number

The mineralization of TB dye increased steadily with an irradiation time up to 78%. However, the photocatalytic degradation of TB over the Mn-doped ZnO nanoparticles was evaluated using pseudo-zero-order (Equation 9), pseudo-first-order (Equation 10), and pseudo-second-order (Equation 11) kinetic schemes, and the results are illustrated in Figure 15. As can be seen, the process agreed with pseudo-first-order model ($R^2$ = 0.9929) with an apparent rate constant ($k_{app}$) of 0.0254 $min^{-1}$. The rate constant corresponding to each equation was obtained from the slope. The rate constant ($k$) and half-life ($t_{½}$) obtained in this study are presented in Table 9.

## 4. Conclusion

The photoresponsive Mn-doped ZnO nanoparticles were prepared using the co-precipitation method. The obtained nanoparticles were characterized using XRD, SEM, EDX techniques. The UV-Vis spectrophotometry was employed to determine the structural, morphological, and elemental properties, as well as band gap values. Based on the XRD, SEM, and UV-Vis analyses, the synthesized Mn-doped ZnO photocatalyst was matched with that of the hexagonal wurtzite structure. The particle size, specific surface area, and band gap values were found to be 24.38nm, 58.27$m^2g^{-1}$, and 3.09eV, respectively. The optimum degradation efficiency of 96.75% was achieved at 15.00mg/L of TB, 0.10g/L of Mn-doped ZnO catalyst, initial pH of 10.00, and 160 minutes of irradiation. Finally, the photodegradation of TB dye over the Mn-doped ZnO nanoparticles fit pseudo-first-order kinetics with the apparent rate constant ($k_{app}$) of 0.0254 $min^{-1}$

## Declarations

### *Competing interests*

There was no conflict of interest between the authors of this work.

### *Authors' contribution*

All authors participated in data collection, preparation of the manuscript, interpretation of results, review, and preparation of the revised manuscript.

### *Funding*

This work received no external funding.

### *Availability of data and materials*

The manuscript contains all datasets generated and/or analyzed in the current study.

### *Ethical considerations*

The authors checked the plagiarism and consented to the publishing of the article. The authors have also checked the article fabrication, double publication and redundancy.

### *Acknowledgments*

The authors thank to the Department of Applied Chemistry, Faculty of Physical Science Federal University Dutsin-ma, Katsina state for providing most of the necessary equipment required for this study.

## References

1. Chong MN, Jin B, Chow CWK, and Saint C. Recent developments in photocatalytic water treatment technology- A review. Water Res. 2010; 44(10): 2997-3027. DOI: 10.1016/j.watres.2010.02.039
2. Robinson T, McMullan G, Marchant R, and Nigam P. Remediation of dyes in textiles effluent: A critical review on current treatment technologies with a proposed alternative. Bioresour Technol. 2001; 77(3): 247-275. DOI: 10.1016/S0960-8524(00)00080-8
3. Zeydouni G, Kianizadeh M, and Khaniabadi YO. Dye removal from aqueous environment by surfactant modified clay: Equilibrium, kinetics, isotherm and thermodynamics studies. Toxin Reviews. 2018;

1551: 1-11.
4. Ramalingam G, Perumal N, Priya AK, and Rajendran S. A review of graphene-based semiconductors for photocatalytic degradation of pollutants in wastewater. Chemosphere. 2022; 300:134391. DOI: 10.1016/j.chemosphere.2022.134391
5. El Saliby IJ, Shon H, Kandasamy J, and Vigneswaran S. Nanotechnology for wastewater treatment: in brief. Encyclopedia of life support system (EOLSS). 2008;7:15. https://www.desware.net/sample-chapters/d13/E6-144-23.pdf
6. Benkhaya S, El Harfi S, and El Harfi A. Classifications, properties and applications of textile dyes- A review. Appl J Envir Eng Sci. 2017; 3(3): 311-320. Available at: https://revues.imist.ma/index.php/AJEES/article/download/9681/5678
7. Woo YS, Rafatullah M, Al-Karkhi AFM, and Tow TT. Removal of terasil red r dye by using fenton oxidation: A statistical analysis. Desalin Water Treat. 2014; 52(22-24): 4583-4591. DOI: 10.1080/19443994.2013.804454
8. Ahani M, Khatibzadeh M, and Mohseni M. Studying the Adsorption Behavior of a Disperse Dye on Polyethylene Terephthalate in Absence and Presence of a Nanostructure Hyperbranched Polymer. Prog Color Color Coat. 2014; 7(1): 49-60. Available at: https://pccc.icrc.ac.ir/article_75818.html
9. Wong PW, Teng TT, and Nik Norulaini NAR. Efficiency of the coagulation-flocculation methods for the treatment of dye mixtures containing disperse and reactive dye. Water Qual Res. 2007; 42(1): 54-62. DOI: 10.2166/wqrj.2007.008
10. Gzar HA, and Sabri NQ. Removal of terasil blue dye from synthetic wastewater using low-cost agro-based adsorbents. Al-Qadisiyah J Eng Sci. 2022; 11(2): 246-255. Available at: https://www.iasj.net/iasj/download/19df1cb66cb49ee7
11. Jaeel AJ. Adsorption of terasil blue on prosopic-farcta: Performance and modelling study. IOP Conf Ser Mater Sci Eng. 2020; 870: 012085. DOI: https://doi.org/10.1088/1757-899X/870/1/012085
12. Cardoso IMF, Cardoso RMF, and da Silva JCGE. Advanced oxidation processes coupled with nanomaterials for water treatment. Nanomaterials. 2021; 11(8): 82045. DOI: 10.3390/nano11082045
13. Gaya UI Heterogeneous photocatalysis using inorganic semiconductor solids. Dordrecht: Springer; 2014. DOI: 10.1007/978-94-007-7775-0
14. Mukhlish MZB, Najnin F, Rahman MM, and Uddin MJ. Photocatalytic degradation of different dyes using TiO2 with high surface area: A kinetics study. J Sci Res. 2013; 5(2): 301-314. DOI: 10.3329/jsr.v5i2.11641
15. Pathania D, Gupta D, Ala'a H, Sharma G, Kumar A, Naushad M, et al. Photocatalytic degradation of highly toxic dyes using chitoson-g-poly (acrylamide) over ZnS in the presence of solar irradiation. J Photochem Photobiol. 2016; 329: 61-68. DOI: 10.1016/j.jphotochem.2016.06.019
16. Repo E, Rengaraj S, Pulkka S, Castangnola E, Suihkenen S, Sopanen M, et al. Photocatalytic degradation of dyes by CdS microspheres under near UV-and blue LED radiation. Sep Purif Technol. 2013; 120: 206-214. DOI: 10.1016/j.seppur.2013.10.008
17. Tahir MB, Sagir M, Zubair M, Rafique M, Abbas I, Shakil M, et al. $WO_3$ nanostructure based photocatalyst approach towards degradation of rhodamine B dye. J Inorg Organomet Polym Mater. 2018; 28: 1107-1113. DOI: 10.1007/s10904-017-0771-x
18. Fardood ST, Forootan R, Moradnia F, Afshari Z, and Ramazani A. Green synthesis, characterization and photocatalytic activity of cobalt chromite spine nanoparticles. Mater Res Express. 2019; 7: 015086. DOI: 10.1088/2053-1591/ab6c8d
19. Akpan UG, and Hameed BH. Parameter affecting the photocatalytic degradation of dyes using $TiO_2$ - based photocatalysts: A review. J Hazard Mater. 2009; 170: 520-529. DOI: 10.1016/j.jhazmat.2009.05.039
20. Kaur J, and Singhal S. Highly robust light driven ZnO catalyst for the degradation of Eriochrome Black T at room temperature. Superlattices Microstruct. 2015; 83: 9-21. DOI: 10.1016/j.spmi.2015.03.022
21. Daneshvar N, Salari D, and Khataee AR. Photocatalytic degradation of Azo dye acid red 14 in water on ZnO as an alternative catalyst to $TiO_2$. J Photochem Photobiol A. 2004; 162(1-2): 317-322. DOI: 10.1016/S1010-6030(03)00378-2
22. Dodoo-Arhin D, Asiedu T, Agyei-Tuffour B, Nyankson E, Obada D, and Mwabora JM. Photocatalytic degradation of rhodamine dyes using zinc oxide nanoparticles. Mater Today: Proc. 2021; 38(2): 809-815. DOI: 10.1016/j.matpr.2020.04.597
23. Algarni TS, Abdah NAY, Kahtani AA, and Aoussi. Photocatalytic degradation of some dyes under solar light irradiation using ZnO nanoparticles synthesized from rosmarinus officinalis extract. Green Chem Lett Rev. 2022; 15(2): 460-473. DOI: 10.1080/17518253.2022.2089059
24. Karnan T, and Selvakumar SAS. Biosynthesis of ZnO nanoparticles using rambutan (Nephelium Lappaceum L) peel extract and their photocatalytic activity on methyl orange dye. J Mol Struct. 2016; 1125: 358-365. DOI: 10.1016/j.molstruc.2016.07.029
25. Khan SA, Noreen F, Kanwal S, Iqbal A, and Hussain G. Green Synthesis of ZnO and Cu doped ZnO nanoparticles from leaf extract of abutilon indicum clerodendrum infortunatum, clerodendrum inerme and investigation of their biological and photocatalytic activities. Mater Sci Eng: C. 2018; 82: 46-59. DOI: 10.1016/j.msec.2017.08.071
26. Ullah R, and Duttah J. Photocatalytic degradation of organic dyes with Mn-doped ZnO nanoparticles. J Hazard Mater. 2008; 156(1-3): 194-200. DOI: 10.1016/j.jhazmat.2007.12.033
27. Djuistic AB, Leung YH, Choy WCH, Cheah KW, and Chan WK. Visible photoluminescence in ZnO tetrapod and multipod structure. Appl Phys Lett. 2004; 84(14): 2635-2637. DOI: 10.1063/1.1695633
28. Abdollahi Y, Abdullahi H, Zainal Z, and Yusof NA. Synthesis and characterization of Mn-doped ZnO nanoparticles. Int J Appl Sci. 2011; 11(4): 44-50. Available at: https://citeseerx.ist.psu.edu/document?repid=rep1&type=pdf&doi=c072ade3dd499b0c0cb72db8bba0b563b98aec53
29. Luo X, Lee WT, Xing G, Bao N, Yonis A, Chu D, et al. Ferromagnetic ordering in Mn-doped ZnO nanoparticles. Nanoscale Res Lett. 2014;9(1):625. **DOI:** 10.1186/1556-276X-9-625.
30. Pazhanivelu V, Selvadurai AP, Zhao Y, Thiyagarajan R, and Murugaraj R. Room temperature ferromagnetism in Mn doped ZnO: Co nanoparticles by co-precipitation method. Physica B Condens Matter. 2016;481:91-6. **DOI:** 10.1016/j.physb.2015.10.10.024
31. Thakur D, Sharma A, Awasthi A, Rana DS, Singh D, Pandey S, et al. Manganese-doped zinc oxide nanostructures as potential scafford for photocatalytic and fluorescence sensing application. Chemosensors. 2020; 8(4): 120. DOI: 10.3390/chemosensors8040120
32. Muhammad AS and Hudu A. Photocatalytic Degradation of Rhodamine B Dye using Mn-doped ZnO Nanoparticles. Appl J Envir Eng Sci. 2022; 8(4): 273-285. DOI: 10.48422/IMIST.PRSM/ajees-v8i4.34946
33. Aadnan I, Zegaous O, El mragui A, Daou I, Mousou H, and da Silver JECG. Structural, optical and photocatalytic properties of Mn-doped ZnO nanoparticles used as photocatalyst for Azo- dye degradation under visible light, Catalysts. 2022; 12(11): 1382. DOI: 10.3390/catal12111382
34. Dhanshree K, and Elangovan T. Synthesis and characterization of ZnO and Mn-doped ZnO nanoparticles. Int J Sci Res. 2015; 4(11): 1816-1820. Available at: https://www.ijsr.net/archive/v4i11/NOV151529.pdf
35. Otadi M, Panahishayegh Z, and Monajjemi M. Synthesis and characterization of ZnO and Mn-doped ZnO nanoparticles and degradation of pyridine in a batch reactor using taguchi experimental designing and molecular mechanic simulation. Biointerface Res Appl Chem. 2021; 11(5): 12471-12482. DOI: 10.33263/BRIAC115.1247112482
36. Khan SA, Shahid S, Bashir W, Kanwal S, and Iqbal A. Synthesis, characterization and evaluation of biological activities of manganese doped zinc oxide nanoparticles. Trop J Pharm Res. 2017; 16(10): 2331-2339. DOI: 10.4314/tjpr.v16i10.4
37. Hamza A, Fatuase JT, Waziri SM, and Ajayi OA. Solar photocatalytic degradation of phenol using nanosized ZnO and $\alpha$-$Fe_2O_3$. J Chem Eng Mater Sci. 2013; 4(7): 87-92. DOI: 10.5897/JCEMS2013.0162
38. Yusuf AH, and Gaya UG. Mechanochemical Synthesis and Characterization of N-Doped $TiO_2$ for Photocatalytic Degradation of Caffeine, Nanochem. Res. 2018; 3(1): 29-35.
39. Hoffman M, Martin S, Choi W, and Behnemenan D. Environmental applications of semiconductor photocatalysis, Chem Rev. 1995; 95(1): 69-96. DOI: 10.1021/cr00033a004
40. Ezema FI, and Nwankwo UOA. Effect of concentration of Mn-Dopant ions on the structural and optical properties of zinc oxide crystals. Dig J Nanomater Biostructures. 2011; 6(11): 271-278. Available at: https://citeseerx.ist.psu.edu/document?repid=rep1&type=pdf&doi=946ea589eebd5cc6beb04b81c9f7bd0a2adc4c13
41. Wang Y, Zhao X, Duan L, Wand F, Niu H, Guo W, et al. Structure luminescence and photocatalytic activity of Mn-doped ZnO nanoparticles prepared by auto combustion method. Mater Sci Semicond Process. 2015; 29: 372-379. DOI: 10.1016/j.mssp.2014.07.034
42. Straumal B, Baretzky B, Mazilkin A, Protasava S, Myatiev A, and

Straumal P. Increase of Mn Solubility with Decreasing Grain Size in ZnO. J Eur Ceram Soc. 2009; 29(10): 1963-1970. DOI: 10.1016/j.jeurceramsoc.2009.01.005

43. Chawla S, and Jayanthi SK. Fabrication of ZnO: Mn nanoparticles with organic shell in a highly alkaline aqueous environment. Appl Surf Sci. 2011; 257(7): 2935-2939. DOI: 10.1016/j.apsusc.2010.10.094
44. Yang M, Guo ZX, Qui K, Lang J, Yin G, Guan D, et al. Synthesis and characterization of Mn-doped ZnO column arrays. Appl Surf Sci. 2010; 256(13): 4201-4205. DOI: 10.1016/j.apsusc.2010.01.125
45. Nirmala M, and Liani A. Structural and optical properties of an undoped and Mn doped ZnO nanocrystalline thin Film. Photonics Lett Pol. 2010; 2(4): 189-191. DOI: 10.4302/plp.2010.4.16
46. Mote VD, Purusthotham Y, and Dole BN. Structural, morphological, physical and dielectric properties of Mn doped ZnO nanocrystals synyhesized by sol-gel method. Mater Des. 2016; 96: 99-105. DOI: 10.1016/j.matdes.2016.02.016
47. Tsuzuki T, Smith Z, Parker A, He R, and Wang X. Photocatalytic activity of manganese-doped ZnO nanocrystalline powders. J Aust Ceram Process Res. 2008; 9: 455-462.
48. Shatnawi M, Alsmadi A, M, Bsoul I, Salameh B, Mathai M, Alnawashi G, et al. Influence of Mn doping on the magnetic and optical properties of ZnO nanocrystalline particles. Results Phys. 2016; 6: 1064-1071. DOI: 10.1016/j.rinp.2016.11.041
49. Yan XX, and Xu GY. Effect of sintering atmosphere on the electrical and optical properties of (ZnO) 1-x ($MnO_2$)x NTCR ceramics. Phys B: Condens. 2009; 404(16): 2377-2381. DOI: 10.1016/j.physb.2009.04.045
50. Akhund A, and Habibi-Yangjeh A. Ternaary Magnetic g-$C_3N_4$/$Fe_3O_4$/AgI Nanocomposites: Novel Recyclable Photocatalysts with Enhanced Activity in Degradation of Different Pollutants under Visible Light. Mater Chem Phys. 2016; 174: 59-69. DOI: 10.1016/j.matchemphys.2016.02.052
51. Shellofteh-Gohari M, and Habibi-Yangjeh A. Novel magnetically separable $Fe_3O_4$@ZnO/AgCl nanocomposites with highly enhanced photocatalytic activities under visible light irradiation. Sep Purif Technol. 2015; 147: 194-202. DOI: 10.1016/j.seppur.2015.04.034
52. Wang J, Jiang WJ, Liu D, Wei Z, and Zhu YF. Photocatalytic performance enhanced via surface bismuth vacancy of $Bi_6S_2O_{15}$ core/shell nanowires. Appl Catal B: Environ. 2015; 176-177: 306-314. DOI: 10.1016/j.apcatb.2015.04.022
53. Nirmala M, and Anukaliani A. Structural and optical properties of an undoped and Mn doped ZnO nanocrysatlline thin film. Photonics Lett Pol. 2010;2(4):189-191. DOI: 10.4302/plp.2010.4.16